Observing Secretory Granules with a Multiangle Evanescent Wave Microscope

Alexander Rohrbach
Max Planck Institute for Medical Research, 69120 Heidelberg, Germany

ABSTRACT In total internal reflection fluorescence microscopy (TIRFM), fluorophores near a surface can be excited with evanescent waves, which decay exponentially with distance from the interface. Penetration depths of evanescent waves from 60 nm to 300 nm were generated by varying the angle of incidence of a laser beam. With a novel telecentric multiangle evanescent wave microscope, we monitored and investigated both single secretory granules and pools of granules in bovine chromaffin cells. By measuring the fluorescence intensity as a function of penetration depth, it is possible through a Laplace transform to obtain the fluorophore distribution as a function of axial position. We discuss the extent to which it is possible to determine distances and diameters of granules with this microscopy technique by modeling the fluorescent volumes of spheres in evanescent fields. The anisotropic near-field detection of fluorophores and the influence of the detection point-spread function are considered. The diameters of isolated granules between 70 nm and 300 nm have been reconstructed, which is clearly beyond the resolution limit of a confocal microscope. Furthermore, the paper demonstrates how evanescent waves propagate along surfaces and scatter at objects with a higher refractive index. TIRFM will have a limited applicability for quantitative measurements when the parameters used to define evanescent waves are not optimally selected.

INTRODUCTION

Whenever a light wave is prevented from propagating by an aperture or an interface, the conservation of momentum and energy of a wave causes the generation of an evanescent field. The most popular method of generating these damped fields is total internal reflection (TIR) (Hecht, 1987). The penetration depth (i.e., the distance of $1/e$ decay) of the exponentially decaying intensity ranges between $\lambda/10$ and λ and varies with the incoming phase, i.e., it depends on the relative refractive index and incident angle. Total internal reflection fluorescence microscopy (TIRFM) (Axelrod et al., 1992) is a method of exciting and detecting fluorescently labeled objects near the surface by these thin light sections. Because hardly any background fluorescence is excited, this technique provides a significant improvement in spatial resolution for nonpoint, near-surface structures, even in comparison to differential interference contrast microscopy (DIC) (Inoue, 1987) and optical scanning techniques like confocal microscopy (Pawley, 1995), theta-microscopy (Stelzer and Lindek, 1994), or multiphoton microscopy (Denk et al., 1990), which are additionally limited in temporal resolution.

Illumination of a 3D fluorophore distribution $C(x, y, z)$ by an exponentially decaying evanescent wave with a decay constant $k = 1/d$ leads to the product $C(x, y, z) \cdot \exp(-k \cdot z)$. Detecting (integrating) the fluorescent light with a microscope objective lens leads to an integral expression depending on the decay parameter k. To a good approximation (depending on detection optics) a Laplace transform (Arfken and Weber, 1995) of the object distribution $C(z)$ in the z direction is recorded by sequentially varying the decay constant k from zero to infinity and plotting the collected fluorescence as a function of k.

By calculating the inverse Laplace transform (Arfken and Weber, 1995), the distribution $C(z)$ can be reconstructed with an accuracy in the range of some nanometers (depending on detection optics, z sampling, and noise). This was implemented for a simple (one-dimensional) geometry by Axelrod (1981), Reichert and Truskey (1990), Burmeister et al. (1994), and Ölveczky et al. (1997) to determine cell-substrate distances of the whole x, y plane by assuming top-hat functions for the fluorophore distribution in the z direction (fluorescence is 0 or 1). The same binary dependency along z has been approximated for spherical objects by Oheim et al. (1998a). For more complicated 3D geometries of fluorophore distributions (like spheres), including pixel blurring by imaging, the inverse Laplace transform has not been applied in this way.

Recently, TIRFM has been used for very interesting applications in the observation of processes near the cell membrane (Steyer et al., 1997; see also Oheim et al., 1998b). Secretory vesicles in live chromaffin cells were investigated during the last steps of their exocytotic pathway. Transport, docking, and exocytosis (Almers, 1990; Parsons et al., 1995; Vitale et al., 1995; Albillos et al., 1997) of single secretory granules and pools of granules could be observed with high image quality at the plasma lemma because of the lack of blurring background intensity.

We modified and extended TIRFM in the same application by illuminating dense-core granules with evanescent waves of variable penetration depths. Therefore we developed a new excitation system, applying very fast angular

Received for publication 29 December 1998 and in final form 23 December 1999.

Address reprint requests to Dr. Alexander Rohrbach, European Molecular Biology Laboratory (EMBL), Meyerhofstrasse1, 69117 Heidelberg, Germany. Tel.: +49-6221-387-123; Fax: +49-6221-387-306; E-mail: rohrbach@embl-heidelberg.de.

0006-3495/00/05/2641/14 $2.00

deflection of a laser beam beyond the critical angle to get more information about diameters of granules and their distances from the cell membrane, as well as their mobility and exocytosis. Information about the sizes of granules and, with that, their absolute positions is not delivered by a single-angle measurement (Steyer et al., 1997). Furthermore evanescent waves with large penetration depths loose their well-defined, exponentially decaying excitation properties in chromaffin cells.

Here we present a method of modeling spheres in evanescent fields mathematically, where a defined fluorescence volume delivers information about the size and the position of each granule. We reconstruct the diameters of isolated granules and distances between vesicles inside the cell and the coverslip. We discuss disturbances and consequences of the interaction of the evanescent wave with the vesicles. Furthermore, we explain how to consider the effects of anisotropic emission of dipoles near a dielectric interface as well as demands on the point spread function (PSF) of the fluorescence detection optics. Finally we introduce the concept of the telecentric excitation system and special features of the experimental setup.

THEORY

Properties of evanescent waves

Proceeding on the assumption that electromagnetic fields must be continuous across a dielectric interface, the existence of evanescent fields appears quite logical in the wave representation. In the particle representation, it is somewhat less obvious. It is known that a photon looses momentum $\mathbf{p} = 2\pi \cdot h \cdot \mathbf{k} = 2\pi h \cdot (k_x, k_z)$ after refraction at an interface with refractive indices $n_{ti} = n_t/n_i < 1$ (t, transmitted; i, incident). The transversal momentum $2\pi \cdot h \cdot k_x$ remains constant, whereas the normal momentum $2\pi \cdot h \cdot k_z$ changes according to angle of incidence α_i and ratio of indices n_{ti}. The component k_z becomes complex when a conservation of momentum in both the transversal (x) and normal (z) directions is no longer possible (Rohrbach and Singer, 1998). This is the case for incidence beyond the critical angle, where no momentum can be transferred to the optically thinner medium. The original propagating wave changes to an evanescent one, exponentially damped in z with the decay constant $-ik_z = \beta = (k_x^2 - (2\pi n_t/\lambda)^2)^{1/2} = 1/d$:

$$d(\alpha_i) = \lambda/4\pi \cdot (n_i^2 \cdot \sin^2\alpha_i - n_t^2)^{-1/2} \quad (1)$$

This is the penetration depth of the evanescent wave, which characterizes the intensity behind the interface as $I(z, \alpha_i) = I(0, \alpha_i) \cdot e^{-z/d(\alpha_i)}$. The intensity $I_0 = I(z = 0, \alpha_i)$ directly behind the interface is described by the Fresnel formulas, which lead to (Axelrod et al., 1992)

$$I_{0p}(\alpha_i) = \frac{4 \cdot \cos^2\alpha_i \cdot (2 \cdot \sin^2\alpha_i - n_{ti}^2)}{n_{ti}^2 \cdot \cos^2\alpha_i + \sin^2\alpha_i - n_{ti}^2} \quad (2)$$

for p-polarization, which was used in our setup. I_{0p} reaches 7.16 times the incident beam intensity, when α_i reaches the critical angle because of constructive interference on the side with index n_i (sapphire-water transition). Because $k_z = -i \cdot \beta$, the Fresnel formulae are now complex, resulting in a polarization-dependent phase shift between the incident and reflected fields, which leads to an elliptical polarization of the reflected beam. Separating the transmitted field $\exp(i\mathbf{kr})$ into $\exp(ik_x x) \cdot \exp(-\beta z)$, it can be seen that an amplitude-modulated plane wave propagates parallel to the surface in the x direction. Energy is transported not in the z but in the x direction, with an average energy flux that is described by the real part of the Poynting vector $\mathbf{S} = c/4\pi \cdot (\mathbf{E} \times \mathbf{H}^*)$ (Axelrod et al., 1992). The energy flux is also parallel to the surface and can be described as $S_x(\alpha_i) \propto I_{0p}(\alpha_i) \cdot \sin\alpha_i \cdot \exp(-\beta z)$. This means that any penetration of objects inside the evanescent wave occurs from the side, not from the top, as is often assumed. For this reason, if the objects have a different refractive index relative to their surrounding, any scattering (i.e., refraction and reflection) of "evanescent" photons occurs in the propagation direction of this surface wave.

This effect was demonstrated by attaching a live chromaffin cell to the interface, as shown in a bright-field recording in Fig. 1 *a*. The cell contained plenty of secretory granules. Surrounded with an aqueous solution ($n = 1.33$) stained with fluorescein, the cell was illuminated with an evanescent wave with a very short penetration depth ($d = 70$ nm). A dark spot indicates the contact area of the cell, where no dye could diffuse between it and the sapphire plate (Fig. 1 *b*). By increasing the penetration depth to $d = 160$ nm (Fig. 1 *c*) and $d = 230$ nm (Fig. 1 *d*), scattering at the optically denser cell (granules) in the propagation direction occurred. The cell with granules ($n \approx 1.37$–1.39) works like a spherical lens, focusing the evanescent wave in such a way that the fluorescent light could be seen as a tail. This scattering effect of evanescent fields has been investigated theoretically with a rigorous electromagnetic calculation by Chew et al. (1979) and with a ray optics approach by Prieve and Walz (1993).

Effects and demands on detection optics

It is the aim here to generate a defined exponentially decaying intensity volume $I(x, y, z, d) = I(x, y, 0, d) \cdot e^{-z/d}$ for excitation and a defined volume in which fluorophore detection takes place. In a homogeneous medium, this detection volume is defined by the point spread function PSF(x, y, z) of the microscope objective with numerical aperture $NA = n_t \cdot \sin\theta$. ($\theta$ is the angle with the optical axis, under which a light beam can be captured by the objective lens.) If there is a dielectric interface (usually a coverslip) close to the fluorophores, this probability of detection via the objective lens is altered by the reflection and refraction of emitted fluorescence photons at the optically denser medium (sap-

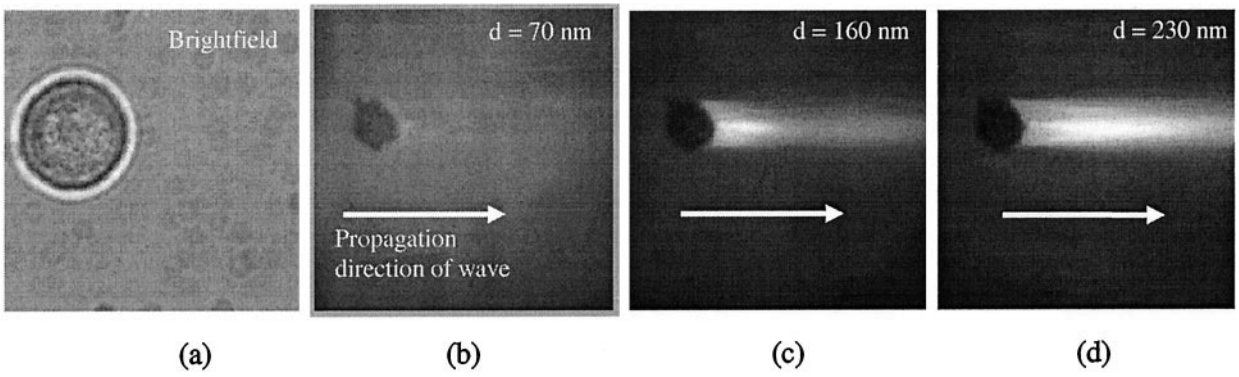

FIGURE 1 (*a*) Bright-field illumination of a live chromaffin cell in a solution containing fluorescein. (*b*) Evanescent illumination with a short penetration depth of $d = 70$ nm, where a dark spot indicates the contact area of the cell. (*c* and *d*) Evanescent waves with larger penetration depths of $d = 160$ nm and $d = 230$ nm are scattered by the granules of the cell, which have a higher refractive index than the aqueous solution. Thus the cell with its granules behaves like a spherical lens. The arrow indicates the propagation direction of the evanescent wave. The image size is 50×50 μm.

phire). This effect is described by the collection efficiency $Q(z)$, which is a function of the distance z.

The point spread function has a clearly defined volume (which is an ellipsoid for a surface of constant intensity of, e.g., 50%), with a finite depth of focus in the z direction. The defined volume and, with that, its elongations are lost when the optical path lengths of the detection light are altered by any refractive index mismatch. This is the case when biological material with a nonhomogeneous refractive index (like chromaffin cells) lies between the object (e.g., the granule) and the objective lens.

We investigated the influence of the finite volume of the PSF on two of its tasks. The one is to integrate as uniformly as possible in the z direction; the other is to resolve as well as possible in the x direction. Fig. 2 shows the sapphire system consisting of the half-cylinder, and the plate where the evanescent field arises after TIR. The shape of a adherent cell is outlined. Excited fluorophores emit photons, which are then focused on the CCD camera with a probability that is proportional to the PSF amplitude. This is indicated in Fig. 2 by the detection volumes of the PSF, i.e., the images of the granules. If we specify that all fluorophores in the z direction are imaged with the same brightness, we require a nearly constant detection probability of 90–100% of the axial PSF amplitude of an ideal lens (here NA = 1.2). From Rayleigh's theory (Hecht, 1987) the depth of focus Δ_z at 90% intensity I, $\Delta_z(I = 90\%)$, is 384 nm at an emission wavelength of $\lambda_{em} = 640$ nm (acridine orange). The corresponding full-width half-maximum (FWHM) in the lateral direction is $\delta_x(I = 0.5) = 325$ nm and defines the minimum distance at which two adjacent spheres can be separated. For latex beads with $\lambda_{em} = 515$ nm, we expect $\Delta_z(0.9) = 309$ nm and $\delta_x(0.5) = 262$ nm. In the experiment, a z scan of a 93-nm bead (taken as a point source) revealed a $\Delta_z(0.9) = 360$ nm and $\delta_x(0.5) = 290$ nm in pure water. A change of the PSF distribution is expected (e.g., because of coma), because the objects have to be detected through water and through the cell, which has a higher refractive index and thus deflects rays. In an additional experiment we allowed beads to diffuse between an adherent cell and the coverslip (sapphire plate) and again recorded the resulting

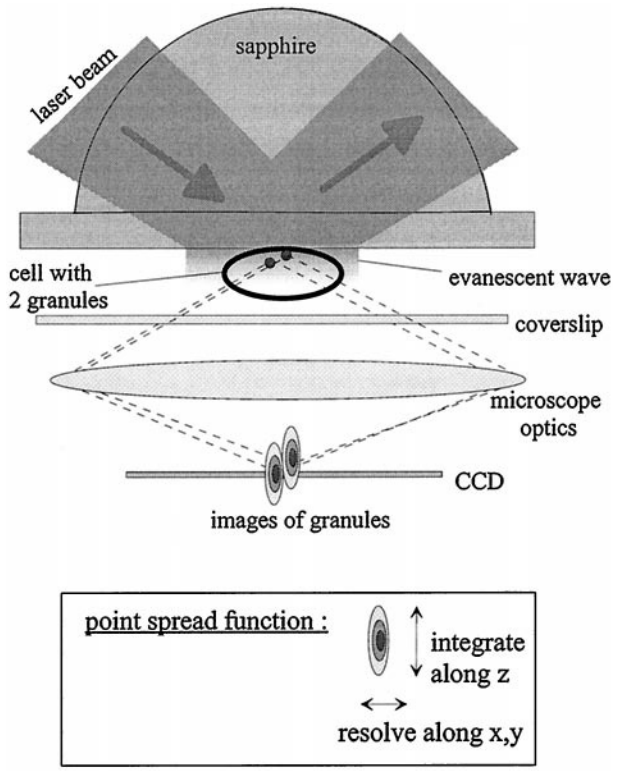

FIGURE 2 Detection of fluorescence emission close to the sapphire interface, where the evanescent field arises after total internal reflection. Granules are detected through the cell, which has a higher refractive index than the aqueous solution. The point spread function, which is influenced by two effects (explained in the text), has the task of integrating as uniformly as possible along the z direction and of resolving as well as possible along the lateral directions.

PSF. We found an increase in the PSF extension of ~10% in both the lateral and axial directions. The experiments indicate that nearly all fluorophores excited with an evanescent wave with penetration depth $d < 250$ nm are detected with an equal probability in z (neglecting the collection efficiency). Thus in further calculations the influence of the PSF in the z direction can be omitted.

Although the influence of the limited depth of focus is negligible, another effect of fluorophore detection plays an important role: The collection efficiency $Q(z)$, describing the nonuniform emission of fluorophores near dielectric surfaces, is defined by the ratio of collected power to total dissipated power of a dipole. As every dipole emits propagating and evanescent fields itself, part of the emitted power is lost as energy is taken out of the dipole's near field, which results in propagating waves under supercritical angles in the medium with a higher refractive index. Because a constant-power (variable-amplitude) dipole must be assumed, this near-field energy absorption is at the expense of those propagating waves that would be collected by the objective. As an additional effect, the emitted far field is partly reflected at the interface and interferes with light coming directly from the dipole. $Q(z)$ depends strongly on the polarization of the excitation light, the orientation of the dipoles, and the configuration of the optical setup (refractive indices, NA, and detection direction of the objective lens). A detailed mathematical description can be found in Lukosz and Kunz (1977), Carniglia et al. (1972), Burghardt and Thompson (1984), and Hellen and Axelrod (1986).

The detected fluorescence $F(x, y, d)$ emitted from the three-dimensional fluorophore distribution $C(x, y, z)$ is a function of space (x, y) and penetration depth d after integration in z. For a pixel (x, y), the following signal can be described as

$$F(x, y, d) = \phi \cdot I_0(x, y, d) \cdot \int_0^\infty [Q(z) \cdot \mathrm{PSF}(z)] \cdot C(x, y, z) \cdot e^{-z/d} dz \quad (3)$$

Here ϕ denotes the quantum efficiencies of the fluorophores and of the CCD camera. ϕ and the fraction of self-absorption in the probe are assumed to be constant. $I_0(x, y, d)$ is defined by Eq. 2. As discussed above, the detection probability PSF(z) can be set to 1 in our configuration, because it is nearly constant over the extension of the evanescent wave, which is ~2 × penetration depth ($\Delta_z(I = 0.9) \approx 2d$).

The influence of the collection efficiency $Q(z)$, which has been computed numerically and multiplied with two different exponentially decaying fields (excitation intensities), is illustrated in Fig. 3. Up to a z distance of 150 nm, fluorescence is diminished considerably by the nonlinear $Q(z)$. For

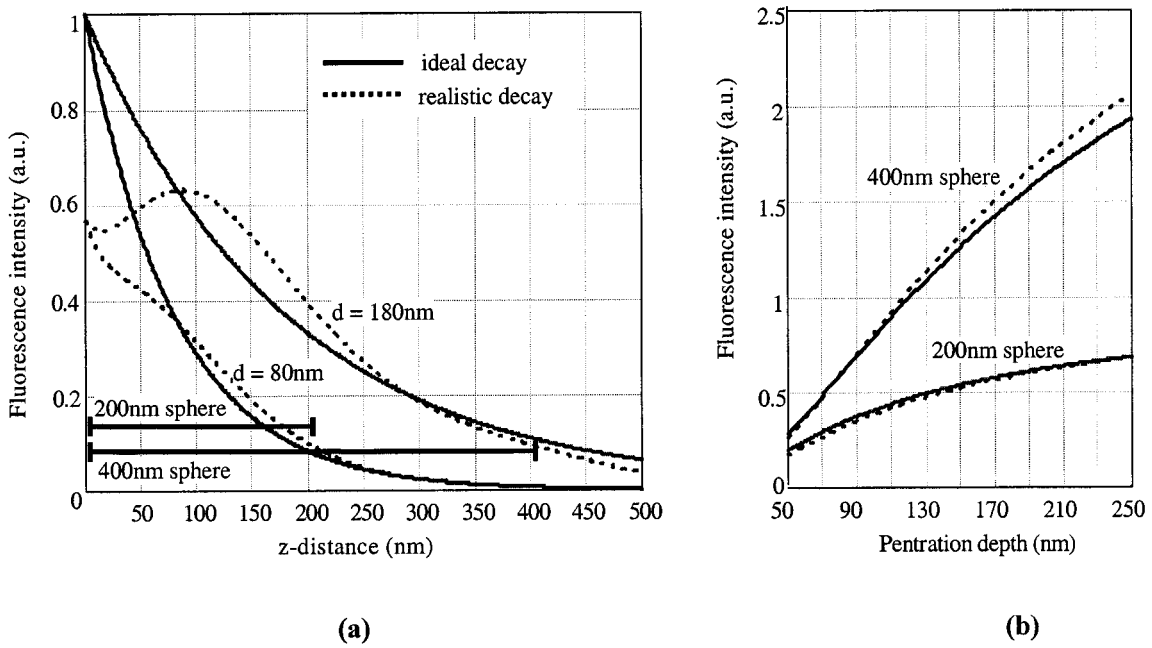

FIGURE 3 (*a*) The extensions of two spheres (*horizontal bars*) with diameters $2 \cdot R = 200$ nm and $2 \cdot R = 400$ nm illustrate the dimensions of the evanescent fields. Fluorescence intensities $Q(z) \cdot \exp(-z/d)$ are shown for collection efficiencies $Q(z) = \text{const.}$ (*solid lines*) and for the nonconstant $Q(z)$ (*dotted lines*) with penetration depths $d = 80$ nm and $d = 180$ nm. (*b*) The effect of the nonconstant $Q(z)$ (*dotted lines*) on the fluorescence volumes of the two spheres touching the interface, compared with a constant $Q(z) = 0.3$ (*solid lines*). The upper curves represent the fluorescence volume of the larger sphere, the lower curves that of the smaller sphere, as a function of penetration depth.

distances $z > 150$ nm its decrease approximates an exponential decay.

Fluorescence volumes of spheres in evanescent fields

Elimination of the surface intensity I_o

Our aim is to reconstruct the fluorophore distribution $C(x, y, z)$, which is the only unknown function in Eq. 3. Here we have to calculate $Q(z)$ numerically (see previous section), because it cannot be measured. The term $\exp(-z/d)$, generated by the evanescent wave, can be adjusted by the angle of incidence of the laser. Integration in z is performed by the objective lens, so that $F(x, y, d)$ is measured by the CCD camera. The quantum efficiency ϕ is assumed to be equal for all penetration depths and can be set equal to 1.

The unknown function $I_0(x, y, d)$ could be calculated according to Eq. 2. However, this would not consider possible irregularities of the setup, such as the angle-dependent transmission of light through the lenses, and of the acoustooptic beam deflector (AOBD), which both influence $I_0(x, y, d)$. Thus we determined $I_0(x, y, d)$ by measuring the fluorescing volume $I_{uni}(x, y, d)$ of a uniform distributed solution of fluorescein with the concentration $C(x, y, z) = c_{FL}$. This integrated intensity is

$$I_{uni}(x, y, d) = c_{FL} \cdot I_0(x, y, d) \cdot \int_0^\infty Q(z) \cdot e^{-z/d} dz$$

$$= c_{FL} \cdot I_0(x, y, d) \cdot DQ(d) \qquad (4)$$

Because it is constant for all penetration depths d, c_{FL} was arbitrarily set to 1. The surface intensity I_0 at $z = 0$ can now easily be determined by $I_0(x, y, d) = I_{uni}(x, y, d)/DQ(d)$. For an ideal collection efficiency $Q(z) = 1$, we would find the integral $DQ(d) = d$. Equation 3 can then be normalized by $I_0(x, y, d)$. For a constant $Q(z) = 1$, the measured (and normalized) fluorescence F in Eq. 3 is the Laplace transform in z of the spatial distribution $C(z)$, when the decay constant $k = 1/d$ is varied. For a nonconstant $Q(z)$, the integrals must be evaluated numerically.

Fluorescence volumes of spheres

For simplicity, we assume that secretory granules are spherical. Then the fluorophore distribution $C(x, y, z)$ can be described by the following three parameters: the center distance a to the interface, the radius R of the sphere, and the fluorophore amount inside, described by c. In other words, the concentration $C(x, y, z) = c$ is assumed to be constant if $[x^2 + y^2 + (z - a)^2]^{1/2} \le R$, whereas $C(x, y, z) = 0$ otherwise (outside the sphere). The fluorescence is detected and integrated over the whole spherical volume according to the product of collection efficiency and excitation intensity as a density function inside the sphere: $Q(z) \cdot \exp(-z/d)$. This approach, in which the excitation field inside the sphere is equal to the incoming field, is known as the First Born Approximation. After eliminating I_0, we write for the intensity per pixel $I(x, y, d) = F(x, y, d)/(I_0(x, y, d) \cdot \phi)$, and after total integration over (x, y) we define $I_d := \int I(x, y, d) dx\, dy$. In cylindrical coordinates:

$$I_d(a, R, c) = c \cdot 2\pi \cdot \int_0^{\sqrt{R^2 - z^2}} \int_{-R}^{R} Q(z) \cdot e^{-(z+a)/d} \cdot r \cdot dr\, dz$$

$$= c \cdot \pi \cdot \int_{-R}^{R} Q(z) \cdot e^{-(z+a)/d} \cdot (R^2 - z^2) dz \qquad (5)$$

For a constant collection efficiency $Q(z) = 1$, this integral can be solved analytically to $I_d(a, R, c) = 4\pi \cdot c \cdot \exp(-a/d) \cdot d^3 \cdot [R/d \cdot \cosh(R/d) - \sinh(R/d)] = I_d^{mes}$. This is an equation with three unknown parameters that can be solved if at least three equations $I_{d1}(a, R, c) = I_1^{mes}$, $I_{d2}(a, R, c) = I_2^{mes}$, and $I_{d3}(a, R, c) = I_3^{mes}$ are known. The inhomogeneity I_d^{mes} is the measured (and normalized) fluorescence intensity of a sphere in an evanescent field with penetration depth d. Unfortunately, I_d^{mes} is intrinsically inaccurate, because of noise and measurement uncertainty, and because the penetration into the sphere (the fluorescence volume) is not well known. Thus, in addition to Eq. 5, the relation between the expected intensity $I_d(a, R, c)$ and the measured intensity I_d^{mes} is described by

$$I_d(a, R, c) = I_d^{mes} + \delta I_d^{mes} \approx I_d^{mes} \qquad (6)$$

The index d denotes the intensities of the different penetrations depths. The additional contribution δI_d^{mes} now requires more than three equations and three measurements, to find the triplet (a, R, c). The error δI_d^{mes} will be discussed in the Results. To estimate the dimensions of spheres in the decaying field and to estimate the influence $Q(z)$, Fig. 3 *a* shows the product $Q(z) \cdot \exp(-z/d)$ with different penetration depths d. Here the solid lines represent the case $Q(z) =$ constant, and the dotted lines illustrate the realistic case of a nonlinear $Q(z)$. Two different bars show the expansion of two spheres $a = R = 100$ nm and $a = R = 200$ nm, touching the interface at $z = 0$. A worst-case estimate of the influence of $Q(z)$ on a defined fluorescence volume can be found from spheres touching the interface. In Fig. 3 *b*, a calculation for two spheres (with $R = 100$ nm (*lower curves*) and $R = 200$ nm (*upper curves*)) shows the fluorescence intensity to be dependent on the penetration depth d of the illuminating evanescent wave. According to Fig. 3 *a*, the dotted lines in Fig. 3 *b* represent the case $Q(z) \neq$ const. and the solid lines the case $Q(z) = 0.3$. The curves are quite similar; however, if we compute the relative error in intensities, $\mathrm{Err}(d) = 1 - [I(Q = 0.3)/I(Q = Q(z))]$, we find that $\mathrm{Err}(d)$ is larger for small penetration depths and small

spheres. For example, the relative error is ~22% for small spheres of radius $R = a = 50$ nm but less than ±5% for a medium sphere of $R = a = 150$ nm.

Determining distances of granules in cells

To minimize movement of granules during measurements, experiments with only two pictures I_1 and I_2 of granules were performed. The corresponding penetration depths are d_1 and $d_2 < d_1$. By calculating the quotient of two recordings, it is possible to eliminate the unknown fluorophore concentration c:

$$I(z, d_1)/I(z, d_2) = c \cdot \exp(-z/d_1)/c \cdot \exp(-z/d_2) = \exp(-z/d_{12}) = I(z, d_{12}) \quad (7)$$

We now get a kind of synthetic $1/e$ − depth $d_{12} = d_1 \cdot d_2/(d_2 - d_1)$. For $d_1 = 80$ nm and $d_2 = 130$ nm, $d_{12} = 205$ nm, which are experimentally relevant values. Within the uncertainty of our measurements, we take the analytical solution $I_d(a, R, c)$ for the integral in Eq. 5 with $Q(z) = 1$ (justified in Fig. 3 *b*). For the ratio I_{d1}/I_{d2},

$$\frac{I_{d1}(a, R, c)}{I_{d2}(a, R, c)} \approx \frac{d_1^3 \cdot [R/d_1 \cdot \cosh(R/d_1) - \sinh(R/d_1)]}{d_2^3 \cdot [R/d_2 \cdot \cosh(R/d_2) - \sinh(R/d_2)]} \cdot \frac{e^{-a/d_1}}{e^{-a/d_2}}$$
$$\approx f(R, d_1, d_2) \cdot e^{-a \cdot (1/d_1 - 1/d_2)}$$
$$\approx (B \pm \Delta B) \cdot e^{-a/d_{12}} \quad (8)$$

The term $\exp(-a/d_{12})$ exclusively describes the center distance a, and the term $f(R, d_1, d_2)$ describes the radius R at penetration depths d_1 and d_2. The term f can be calculated as a function of R for different parameters a. The result is a weak descending function, allowing the approximation $f(R) \approx B =$ constant, and we accept an error of $\Delta B < 20\% \cdot B$ by assuming a mean granule radius of $R = 180$ nm for all vesicles.

There is background fluorescence $U(x, y)$ in every image $I(x, y)$ due to fluorescing objects at larger distances from the coverslip which are excited and detected by the tails of the evanescent wave and the PSF. We remove the background $U(x, y)$ by high-pass Gauss filtering (Appendix).

As an example, we took two pictures I_1 and I_2 with $d_1 = 80$ nm and $d_2 = 130$ nm (thus $d_{12} = 205$ nm), where no scattering effect could be detected. The ratio leads to the dependency $I_{12} = I_{max} \cdot \exp(-a/d_{12}) \approx I_{max} \cdot (1 - a/d_{12})$ in first-order Taylor or $a' = a + R \approx d_{12} \cdot (1 - (I_{12}/I_{max}) +$ 180 nm. Here I_{max} is the maximum intensity of $I_{12}(x, y)$ that leads to the minimum center distance of a granule. The minimum center distance should be at least the mean radius of the granules $R = 180$ nm ($a' = a + R$). A linear approximation (first-order Taylor) is justified for a center distance of up to $d_{12} + R$.

Determining diameters of isolated granules

We assume that isolated granules touch the interface, so that the center distance $a =$ radius R. To eliminate the effect of the varying fluorophore concentration c, we again take the quotient of two recordings. Here all the intensities will be normalized to the intensity $I_{100}(a = R)$ at a penetration depth of $d = 100$ nm. Because only isolated granules are treated, we are able to integrate the intensity easily over the whole spot area. According to the model presented in Eq. 5, we expect the following relative intensity volume $I_{d/100}$ for spheres touching the interface ($a = R$):

$$I_{d/100}(a = R) = \frac{\int_{-R}^{R}(R^2 - z^2) \cdot Q(z + R) \cdot e^{-(z+R)/d} dz}{\int_{-R}^{R}(R^2 - z^2) \cdot Q(z + R) \cdot e^{-(z+R)/100} dz} \approx I_{d/100}^{mes} \quad (9)$$

By measuring the volume I_d^{mes} for different penetration depths d and normalizing them to I_{100}^{mes}, we can reconstruct the last unknown parameter R. Because our data are noisy, we plot the relative intensity volumes $I_{d/100}^{mes}$ against the penetration depth d (a Laplace transform is usually plotted against $k = 1/d$) and perform a best fit with χ^2 minimization. The minimum of the error $E(R) = \Sigma(I_{d/100}(R) - I_{d/100}^{mes})^2$ leads to the most probable radius R of the granule.

INSTRUMENTATION

Excitation optics

Fast variation of evanescent field penetration depths requires at least one active element for deflection of the laser beam and, second, a configuration of passive optical components for coupling the beam under supercritical angles onto a single point of the interface. This second task was implemented with a telecentric system (Rohrbach, 1998), a configuration also used later on by Oheim et al. (1998a). For the interface, we chose sapphire with index $n_s = 1.78$ as a high refracting medium. This allows us to generate evanescent waves with penetration depths from ~40 nm to 300 nm in aqueous solution ($n = 1.33$) at an excitation wavelength of 488 nm from a 15-mW argon-krypton laser (643-AP-A01; Omnichrome). As an active deflection element we employed an acoustooptic beam deflector (AOBD) (N45100–3-6.5DEG, NEOS) with a maximum deflection range of 37 mrad (= 2.2°) and a repositioning time of less than 0.5 ms. With two achromatic lenses (Spindler and Hoyer; $D = 30$ mm in diameter) with focal lengths $f_1 = 1330$ mm and $f_2 = 200$ mm, we achieved a magnification of the deflected angles of $f_1/f_2 = 6.65$ (see Fig. 4). As long as the beam diameter is at least one order of magnitude smaller than the diameter of the lenses, the two lenses need not necessarily form a conventional telecentric system, because the distance between them can be much smaller than $f_1 + f_2$. When two lenses are used, the first can easily be adjusted to the deflection range of the active element (AOBD or a

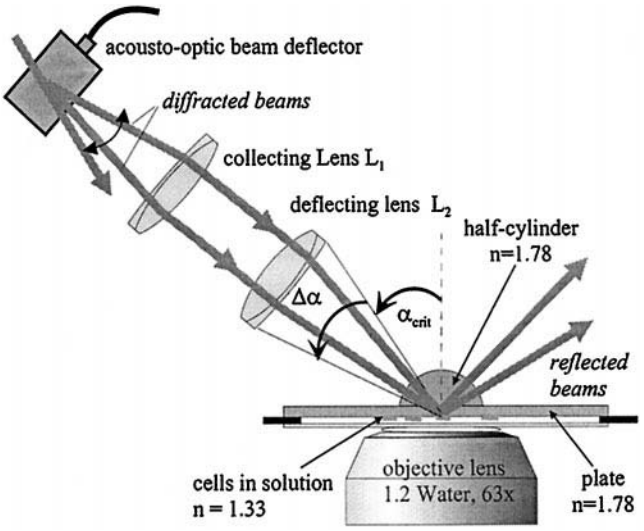

FIGURE 4 The deflection angle of an acoustooptic beam deflector is magnified by a telecentric system. Together with a half-cylinder, beams are deflected and focused under different supercritical angles into the center of the image field of the objective. Evanescent fields of various penetration depths are generated within the range $\Delta\alpha$ of supercritical angles. Cells are mounted in a perfusion chamber and are observed through water.

tilting mirror), and the second lens can be chosen to easily adjust the necessary angle magnification (the range $\Delta\alpha$). To avoid longitudinal spherical aberrations that lead to different x, y positions of the evanescent wave, we used only 90% of the lens aperture. Within a range of angles of $\Delta\alpha = 7.7°$, different evanescent decays beyond the critical angle $\alpha_{crit} = 48.35°$ could be generated. We chose a half-cylinder ($R_{Cyl} = 5$ mm) for the transition from air to sapphire (perpendicular incidence) to avoid a change of incident angles by refraction (Fig. 4). The height of the half-cylinder was shortened by the thickness of the sapphire substrate (1 mm), so that every incident laser beam within $\Delta\alpha$ had the same optical path length from the deflecting lens surface to the focus region (region of evanescent waves). For index matching between half-cylinder and plate (transducer) we used *D*iiodide *M*ethane, with $n_s = 1.78$. The half-cylinder (coated on the air/sapphire interface against internal reflections) was fixed with a special holder, while the transducer with attached fluorescing particles could be moved with a stepper motor, so that it could slide under the thin film of the index matching fluid.

Beam forming

The naturally diverging laser beam converges after passing the lenses and the half-cylinder. This influences the spot size of the laser beam at the interface and produces a set of incident angles, i.e., a superposition of exponential decays of the evanescent field. In the *s* direction (perpendicular to plane of incidence) the 1.2-mm laser beam is focused with the $f_1 = 200$ mm lens down to a diameter of 103 μm ($1/e^2$ intensity), equivalent to 24 μm at 90% intensity. In the *p* direction the spot diameter increases by $1/\cos(\alpha_i)$, according to the oblique incidence angle α_i and decreases by the focusing through the half-cylinder with $f_{Zyl} = (n_s - 1)/n_s \approx 0.44 \cdot R_{Zyl}$. Thus a plane wave will be focused at a distance $0.44 \cdot R_{Zyl}$. The wave incident on the half-cylinder must be divergent to be focused at the bottom of the coverslip at the distance R_{Zyl}. This results in a spot diameter of 20–30 μm at 90% intensity, which is sufficient for a homogeneous illumination of the adherent surface of a chromaffin cell.

We calculated a range of incident angles of 0.57° over the diameter of the laser beam, which was focused by the deflecting lens and the half-cylinder. This Gaussian distribution of incident angles generates a mean exponential decay with a mean penetration depth $d_{mean}(\alpha)$ ($\alpha \in [\alpha_0 - 0.57°/2, \alpha_0 + 0.57°/2]$), which differs by 5% at most from an unfocused incident beam, generating a penetration depth of $d(\alpha_0) = 200$ nm.

Inhomogeneities in the beam intensity can be caused by the interference of unavoidable reflections in the optical system. To reduce these effects, we used a transparent disc rotating at 5500 rpm. The varying optical path length shifts the phase $\phi(x, y)$ by more than 2π within the integration time of the CCD camera. Thus the phase $\phi(x, y)$ and the resulting intensity are averaged.

Detection optics

Illuminated objects close to the interface were detected through water with a water immersion objective lens (Plan-Apochromat 63×, NA = 1.2; Zeiss) in an inverted microscope from Zeiss (Axiovert T135). Further magnification with an Optovar (1×, 1.6×, 2.5×) and by 4 with an additional lens guaranteed high image sampling from the CCD camera. A cooled slow-scan CCD camera (16-bit, back-illuminated) (SI502BA; SITe, Inc.) with a 512 × 512 pixel array (24 × 24 μm pixel size) was used for image recording. Image acquisition at a rate of 3 s^{-1} could be achieved with a 256 × 256 pixel array and 12-bit sampling at 100 ms of illumination time. For z scans and focus stabilization we used a piezo-scanner (P-721.10 PIFOC; Physik Instrumente) together with an external sensor (E-115.21; Physik Instrumente).

The position of the totally reflected laser beam was measured with a 512-pixel CCD line (TSL 218; Texas Instruments). The laser spot of the outgoing beam (~1 mm in diameter) was sampled with eight values; averaging and maximum determination of these eight values led to a good angular resolution (better than 0.1°). The reflected angle α_i (= incident angle) was obtained with the help of the tangent relation $\alpha_i = \arctan(\Delta x/(\Delta z + \Delta p))$. Δx and Δz were measured once with a ruler; the spot movement Δp in the z direction was then measured electronically, using the CCD line.

Electronic setup

The electronic setup has two important tasks: first to control the deflection of angles and thus the evanescent illumination of the probes; second, to collect the fluorescent light with the CCD-camera. The latter was performed with a PC and programmed macroroutines established and implemented in WinView (Visitron Systems GmbH) to acquire image stacks in loops with variable delays. An external TTL signal coinciding with the camera shutter was sent from the camera controller (ST138S; Princeton Instruments) to a separate electronic setup, responsible for the evanescent illumination. This real-time operating system (RTOS) was triggered by the TTL signal and then read out a voltage pair from a table. This voltage pair encodes the diffraction angle and efficiency of the AOBD, which yield the penetration depth of the arising evanescent wave and illumination intensity (between zero and a defined value). Because of the speed of the RTOS and the AOBD, the excitation of the probe starts and stops only with a 0.3-ms delay to the illumination of the CCD camera. The RTOS computer also calculates, monitors, and saves incident angles and penetration depths measured via the CCD line. For non-time-critical applications, the AOBD also could be controlled by two D/A converters on the PC board.

METHODS

We imaged bovine chromaffin cells 2–3 days after they had been plated onto sapphire plates (coated with PDL). Cells were incubated in 135 mM NaCl, 2 mM KCl, 5 mM $CaCl_2$, 2 mM $MgCl_2$, 19 mM Na-HEPES at pH 7.2 at 22–24°C. The resulting potential kept the Ca^{2+} channels closed and secretion did not occur. Cells were stimulated by an influx of 60 mM KCl. Influx of 60 mM KCl with 7 mM $MgCl_2$ instead of $CaCl_2$ allowed vesicles to dock at the plasma membrane but prevented exocytosis. Granules were stained by incubating the cells in 3.0 μM acridine orange for 12 min at 22–24°C.

RESULTS

Evanescent illumination of secretory granules

Scattering signifies a change of direction of the incident **k**-vectors of a wave (of a photon in the particle representation). The evanescent wave, propagating parallel to the *x,y* plane, is not only scattered (focused) in the *x,y* plane, but also in the *z* direction. Thus excitation light is also scattered into deeper regions of the cell by the granules. This effect is illustrated in three images of a chromaffin cell, where fluorescence had been excited by evanescent waves of $d = 65$ nm, $d = 95$ nm, and $d = 155$ nm penetration depth (Fig. 5, *a–c*). A very short penetration depth (Fig. 5 *a*) results in a weak excitation of dye molecules close to the interface. In Fig. 5 *b* the intensity of fluorescing granules is uniform, whereas in Fig. 5 *c* an increase in fluorescence can be seen from left to right (propagation direction of the wave) because of more scattering at a larger number of granules. Averaged horizontal linescans across the whole cell such as those in Fig. 5 *c* reveal an increase in additional fluorescence, which reaches up to 300% after 10 μm of propagation of the wave at a penetration depth of ~150 nm (Fig. 5 *d*). Fluorescence intensity was normalized to an averaged linescan of a record without scattering (as in Fig. 5 *b*). Even for a medium penetration depth of ~115 nm, additional fluorescence caused by scattered light increases by more than 100%. The strength of this effect varies from cell to cell but occurs in all chromaffin cells for penetration depths larger than 150 nm. Additional fluorescence is possible, because excitation energy is taken locally from the other side of the interface, along the extension of the incident beam.

This effect destroys any defined (and desired) exponential decay of an evanescent wave and prevents quantitative analysis of fluorescence when larger penetration depths are

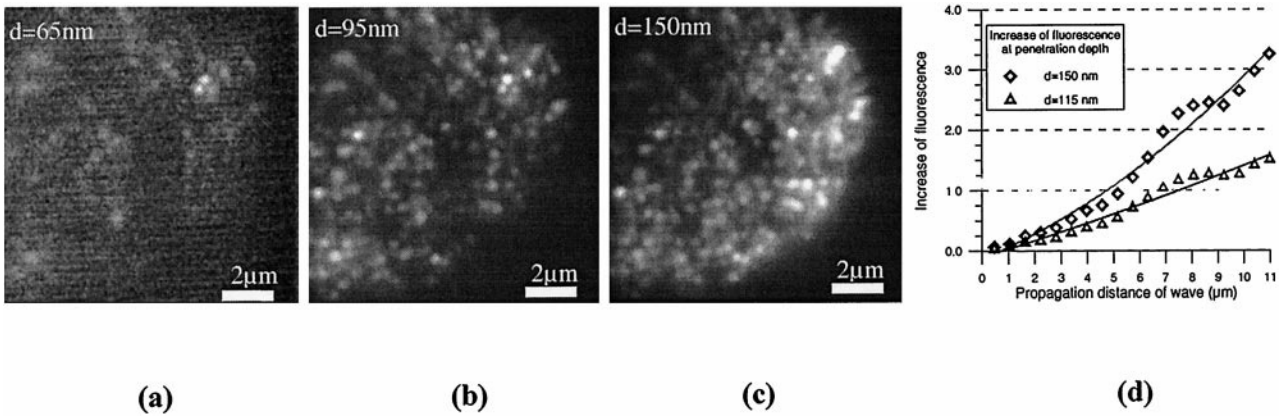

FIGURE 5 Evanescent illumination of secretory granules, with the wave propagating from left to right. The short penetration depth of $d = 65$ nm gave a weak excitation of the close granules (*a*), whereas with $d = 95$ nm, a clear and homogeneous fluorescence of the vesicles could be observed (*b*). Larger penetration depths of $d \geq 140$ nm can lead to inhomogeneous fluorescence (*c*), increasing with the propagation distance of the wave. (*d*) Averaged linescans across the whole cell along the propagation direction of the evanescent wave. Detected fluorescence increases because of scattering of excitation light. The fluorescence intensity is normalized to an averaged linescan of a recording without scattering (as in Fig. 5 *b*).

used. The increasing excitation and fluorescence can be seen clearly when the evanescent wave comes from only one side, but it is hardly noticed when a symmetrical illumination from all sides is used (Stout and Axelrod, 1989; Steyer et al., 1997).

Determining fluorescence volumes of granules

Penetration of the granules

So far it has been assumed that fluorophores are excited with the same intensity inside the granules as outside. This would occur if the protein matrix of the vesicles had the same refractive index as their surroundings. Unfortunately they have an index up to 0.06 higher than that of water. This index step would lead to the supposition that a granule is no longer penetrated exponentially in z, because the internal fields now may obtain propagating components in z or generate resonances inside the granule (Knight, 1995). If we assume an approximately homogeneous density of excitation light inside the granule with a mean intensity $I_{\text{full}}(z) = \exp(-a_0/d)$ at the center distance a_0 (in comparison to an exponential decay $I_{\text{exp}}(z) = \exp(-z/d)$) inside, we can calculate the relative errors of the intensities $I_{\text{exp}}(d)$ and $I_{\text{full}}(d)$. This relative error is small as long as the radii of the granules are not larger than the penetration depth of the illuminating evanescent wave. For larger radii, the integrated fluorescence intensities $I_{\text{exp}}(d)$ and $I_{\text{full}}(d)$ are quite different.

In addition, we performed the following experiment. We illuminated isolated granules (close to the interface), with increasing penetration depths of evanescent waves up to epiillumination ($d \rightarrow \infty$). From the ensuing granule spots, we measured the diameters (FWHM). As expected, we found no significant difference between evanescent and epiillumination for small granules. But for large granules, we measured an increasing FWHM with an increasing penetration depth up to epiillumination. This indicates that with evanescent illumination, only a cap of the sphere fluoresces. This implies that despite the higher index, spheres do not fluoresce homogeneously, but generate a sectional fluorescence according to the penetration depth of the exponentially decaying evanescent wave.

To summarize, the internal fields can be assumed to be equal to their incident external fields (Rayleigh-Gans or Born approximation).

Measuring fluorescence volumes of granules in cells

Equation 6 describes the relation between the measured intensity volumes $I_{\text{d}}^{\text{mes}} + \delta I_{\text{d}}^{\text{mes}}$ on the right-hand side and expected values I_{d} as a function of (a, R, c) on the left-hand side. The error $\delta I_{\text{d}}^{\text{mes}}$ can be categorized as follows, with maximum errors as a percentage of $I_{\text{d}}^{\text{mes}}$: background fluorescence ($\Delta I_{\text{H}} \leq 45\% \cdot I_{\text{d}}^{\text{mes}}$), photon noise ($\Delta I_{\text{R}} \leq 12\% \cdot I_{\text{d}}^{\text{mes}}$), peak intensity ($\Delta I_{\text{A}} \leq 45\% \cdot I_{\text{d}}^{\text{mes}}$), error in surface intensity ($\Delta I_0 \leq 16\% \cdot I_0$), and lateral scattering of excitation light ($\Delta I_{\text{S}} = 0\text{–}300\% \cdot I_{\text{d}}^{\text{mes}}$).

The strongest disturbance ΔI_{S} can be avoided only by using isolated granules or granules in cells with low vesicle density at penetration depths of $d < 150$ nm. Under these conditions, the background intensity can be estimated with the help of a mean signal-to-noise ratio, which can be determined by computing the peak intensity and the local background of a granule spot. The photon noise depends on the exposure of the CCD camera, and here it is smaller than 12%.

The error in surface intensity ΔI_0 is taken to be an instrumental error, which also includes uncertainty in the refractive index of the aqueous cell solution and the spot homogeneity at the interface. For the largest penetration depth used inside cells ($d = 155$ nm), it is at most 16%.

A relation between the total spot intensity and the maximum peak intensity of a spot has been established by convolving the measured PSF of the objective lens with modeled spheres of different sizes. This relation grows quadratically with increasing object radius. Assuming that the total spot intensity is always proportional to the maximum peak intensity, we find a maximum error ΔI_{A} of 45% (a mean error of 20%) for granule diameters from 150 nm to 500 nm.

The total error δI^{mes} for the fluorescence volume is estimated using all of the errors described above and will be used in the next section, where the error of the reconstructed center distances is assessed.

Determining distances of granules in cells

Fig. 3 *a* illustrates the dimensions of evanescent fields and spheres. What happens if these extended objects move along the decaying excitation fields in z and all arising fluorescence is integrated/averaged in the z direction? Assuming an exponential decay of excitation light inside the spheres, we calculated the resulting fluorescence intensities as a function of the center distance a. The result is plotted in Fig. 6, where the decaying behavior of a point source (which is, of course, $Q(z) \cdot \exp(-z/d)$) is compared with spheres of $R = 100$ nm and $R = 200$ nm radius. For two different penetration depths, we find a quite similar behavior. Because we take the center distance, the curves for the spheres start at $a = R = 100$ nm and $a = R = 200$ nm, respectively.

These results allow us to approximate extended spheres as points and to use an exponential fluorescence decay with increasing center distance for approximations that are made together with Eq. 8.

As explained in the Theory section, three unknown parameters a, R, and c for center distance, granule radius, and fluorophore concentration must be determined (Eqs. 5 and 6). A problem occurs because considerably more than three

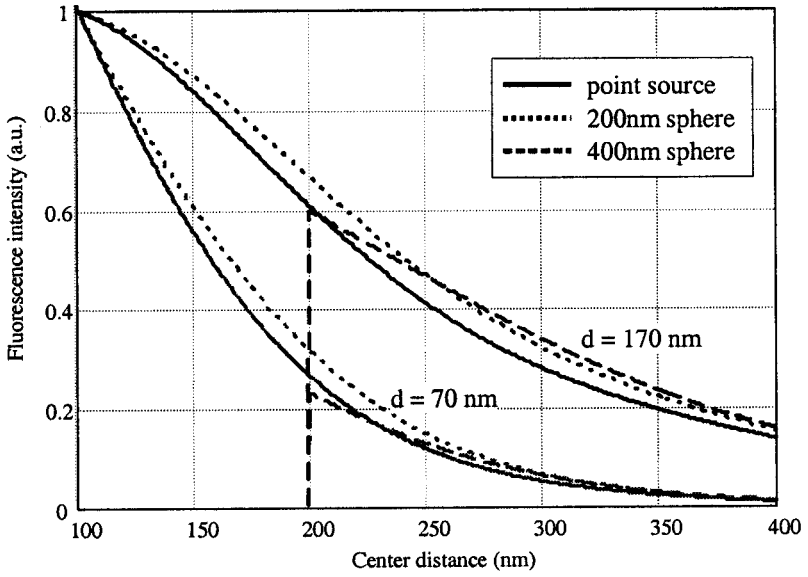

FIGURE 6 Decay of fluorescence intensities with increasing center distance of a point source (——), a 200-nm sphere (·····), and a 400-nm sphere (– – –). All curves are normalized to 1 at z = 100 nm. The lower curves belong to the short penetration depth of d = 70 nm and the upper curves to the large penetration depth of 170 nm.

measurements must be made to determine a, R, and c if $\delta I^{\text{mes}} > 0$; but vesicles move (and bleach) during the acquisition of a series of measurements I_n^{mes}. Another problem is the blurred images of dense granules in cells due to diffraction. Integrating the intensity spots over the whole spot area of one granule is hardly possible. Instead of trying to determine the spot area intensity, we thus take the peak intensity I_A, which is easy to measure. In this case we have to accept a maximum error ΔI_A (described in the preceding section).

To minimize the possible movement of granules during measurements, we performed an experiment with just two pictures, I_1 and I_2, of granules (with two penetration depths d_1 and $d_2 < d_1$). By calculating the quotient, it is possible to eliminate the unknown fluorophore concentration c (see Theory section). The result is shown in Fig. 7 as a pseudo-3D plot, where the center distances of 131 secretory granules are plotted in a circular region 12 μm in diameter. We estimate a relative error of up to 50%.

Determining diameters of isolated granules

It is possible to optically determine isolated granule diameters by deconvolving the spots from the PSF of the objective. With the water-immersion long-distance objective with NA = 1.2, it is possible to distinguish spot diameters down to 300 nm (FWHM), which corresponds to granule diameters of the same size.

To record a Laplace transform and to reconstruct diameters of isolated vesicles, we did the following experiment: we took 20 exposures $I(1)$ to $I(20)$ with different penetration depths of isolated granules from a burst cell, where the first penetration depth was equal to the last. With $I(20) = I(1) \cdot e^{-\alpha \cdot 19}$ or $\alpha = 19 \cdot \ln[I(1)/I(20)]$, we carried out a bleaching correction of the dye (acridine orange). Each spot intensity was divided by $I(10)$ with d = 100 nm according to Equation 9, then plotted as shown in Fig. 8. The error bars result from an assumed 10% error in penetration depth d and from the measured surface intensity $I_0(x, y)$. Three different curves with different gradients represent three different granule radii. In our example of Fig. 8, χ^2 minimization leads to diameters $2R$ = 70 nm, 240 nm, and 300 nm with a small χ^2 or $E(R)$. These granule sizes cannot be determined or resolved with a traditional optical microscope.

DISCUSSION

The purpose of this study was to develop a technique to rapidly vary the penetration depths of evanescent waves and

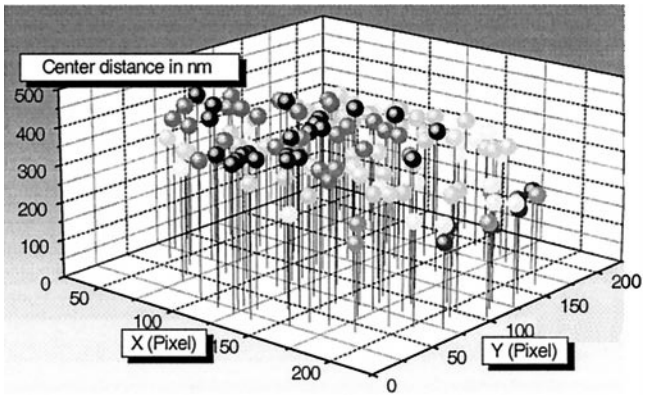

FIGURE 7 Pseudo-3D plot of 131 reconstructed center distances of granules to the coverslip in a live chromaffin cell before stimulation. The minimum possible center distance of granules, i.e., when they touch the surface, is the assumed mean radius R = 180 nm, and the furthest center distance is about $d_{12} + R \approx 400$ nm. The investigated circular region in the lateral domain has a diameter of 12 μm.

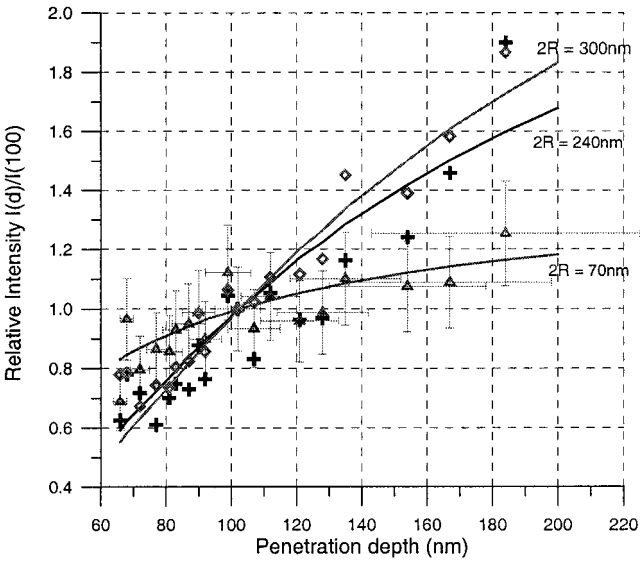

FIGURE 8 Integrated intensity $I_{d/100} = I(d)/I(d = 100\ \text{nm})$ as a function of penetration depth d of three isolated granules touching the interface ($a = R$). The steeper the gradient of the curve, the larger the granule, which is penetrated by the evanescent wave. The best fits belong to diameters of $2 \cdot R = 300$ nm (◇), 240 nm (+), and 70 nm (△). The error bars are shown for only one curve.

to apply this technique to the study of secretory granules in live chromaffin cells. Multi-angle TIRFM had been used before to determine cell-substrate distances (Axelrod, 1981; Reichert and Truskey, 1990; Burmeister et al., 1994; Ölveczky et al., 1997). It is a further aim of this paper to present new methods to investigate spherical objects with evanescent waves and to critically examine difficulties and merits of this microscopy technique.

Instrumentation design

The decisive idea in setting up this novel and fast instrument consists of the combination of a fast beam deflecting active device (AOBD) and two achromatic lenses as deflecting passive devices. This telecentric system is not limited in operation speed and is easy to align because only a magnification of the deflection angle of the active device has to be performed properly (Rohrbach, 1998; Oheim et al., 1998a). Other TIR techniques (Ölveczky et al., 1997; Burmeister et al., 1994) are limited in speed, and their adjustment is more complicated because a laser beam has to be directed and adjusted to one fixed point for every supercritical angle. The choice of a sapphire half-cylinder together with a plane and stable plate of sapphire (as a coverslip) and a matching fluid (diiodide methane) in between guaranteed a simple, accurate, and flexible method of generating total internal reflection. We thus generated areas of evanescent waves that were well centered in the image field of the microscope objective. A refractive index of 1.78 allowed a reasonable range of incident angles, resulting in penetration depths of the evanescent waves from 70 nm to 250 nm. The influence of focusing the laser beam and the change of its shape at the half-cylinder have been investigated with regard to a homogeneous intensity distribution in the illuminating area. The detection optics consisted of a high-performance long-distance microscope objective (NA = 1.2, water) and a sensitive 12-bit slow-scan CCD camera. With an acquisition rate of 3 frames/s, the camera was the speed-limiting factor in the setup. A rate of more than 20 frames/s should be possible with a fast frame-transfer camera, because there is no practical speed limitation for the beam-deflecting optics. An external computer (real-time operating system) allowed a fast and independent control of the laser deflection for an evanescent fluorescence excitation. The spot position of the total reflected beam was measured with a CCD line, guaranteeing the automated and precise measurement of the reflection angle.

Evanescent waves propagate

Our consideration of the characteristics of evanescent waves shows that an evanescent wave behaves like a propagating wave with a nearly exponential amplitude modulation. Thus, in a propagation direction parallel to the interface, it is scattered at obstacles with higher refractive index (such as cells) and loses its originally clearly defined excitation volume. To our knowledge, this effect has never been illustrated before.

Scattering was also shown at stained secretory granules in live chromaffin cells illuminated with evanescent waves at penetration depths of 65 nm, 95 nm, and 155 nm. With increasing penetration depth, the degree of scattering into deeper regions of the cell also became stronger (far beyond the adjusted penetration depth). Depending on the cell and its adhesion to the interface, already at a penetration depth of about $d \approx 140$ nm, the extent of the well-defined intensity volume of the evanescent wave was lost. This is especially the case for a prismless evanescent-wave microscope, where penetration depths are very large (Stout and Axelrod, 1989; Steyer et al., 1997). This limiting effect should be taken into account in all studies of non-point-like objects, where the defined illumination volume of the exponentially decaying evanescent waves is exploited. However, with penetration depths of $d = 60$ nm to $d \approx 130$ nm, a clear and homogeneous evanescent illumination of vesicles could be achieved. Very good results, for example, have been achieved by evanescent illumination of surfaces of cell nuclei due to a lower (optical) density of the chromatin (Rohrbach, 1998).

Demands on detection optics

To investigate the demands on the detection optics of a TIR setup, we defined the FWHM $\delta_x(50\%)$ of the detection point

spread function PSF(x, z) as a criterion for lateral resolution and the 90% intensity of the PSF(x, z) as the necessary depth of focus $\delta_z(90\%)$ in z. The extension δ_z, which should be larger than the penetration depth of the evanescent wave, was defined to achieve a fluorophore detection of approximately equal probability from $z = 0$ to $z = d$. In water, we measured $\delta_x(50\%) = 290$ nm and $\delta_z(90\%) = 360$ nm for latex beads ($\lambda_{em} = 515$ nm), values that are 10–13% broader than the theoretical values according to Rayleigh. For the emission wavelength of acridine orange ($\lambda_{em} = 640$ nm), similar deviations can be assumed. The fluorescence of vesicles excited with evanescent waves had to be detected through the cell. The resulting change of the optical path length and the deterioration of the PSF due to coma had been investigated with beads that diffused between the interface and the cell membrane. We found a broadening of the PSF (caused by observing through the cell) of ~10% along both the x and z directions. Surprisingly, no further work addressing this problem has been presented by other authors working on TIR.

Furthermore, the influence of the nonlinear collection efficiency $Q(z)$ for fluorophores near a dielectric surface was investigated. This was considered in the Theory section by a multiplication of the nonlinear $Q(z)$ (calculated numerically by B. Ölveczky) with different exponential decays $\exp(-z/d)$. A dramatic change in the shape of this fluorescence detection curve from a pure exponential decay for distances $z < 150$ nm could be observed. Only for $z > 150$ nm does the intensity have a kind of exponential decay. This effect must be taken into account when point-like objects are illuminated with evanescent waves!

Measuring and modeling fluorescing granules in evanescent fields

Because we wanted to investigate positions and diameters of the spherical vesicles, we evaluated the integrated intensity of their fluorescence volumes. This intensity $I(x, y, d)$ was normalized for the different penetration depths d, i.e., by dividing by $I_0(x, y, d)$. I_0 was found by measuring the fluorescence volume I_{uni} of a uniform distributed solution of fluorescein. Taking the ratio of the measured intensity volume I_{uni} and the calculated spatial volume of the evanescent wave is the best method for obtaining I_0 (Ölveczky et al., 1997; Oheim et al., 1998). By taking the ratio, we considered all of the effects of intensity fluctuations at the surface, and the most probable volume of the wave was chosen according to penetration depth and angle of incidence.

The fluorescence volumes of spheres in evanescent waves can be described by three parameters: the center distance a, the radius R, and the fluorophore concentration c. We advanced an integral describing this fluorescence volume $I_d(a, R, c)$ for different penetration depths d, which can be solved analytically if the collection efficiency $Q(z)$ is constant and numerically for a nonconstant $Q(z)$. As a worst-case estimate, both fluorescence volumes for $Q(z) =$ const. and $Q(z) \neq$ const. for spheres touching the interface were calculated. We plotted $I(d)$ as a function of penetration depth d, but did not find a large difference between the two cases for $Q(z)$. Only for small spheres ~100 nm in diameter does a difference of up to 22% occur. The influence of $Q(z)$ depends on the refractive index of the transducer (half-cylinder), the NA of the objective lens, and the side on which the detection is performed. This must be calculated for each configuration. A very similar model was presented by Oheim et al. (1998a), where the solution of the 3D integral over the sphere was approximated by a top-hat function for each pixel in the x, y plane. However, neither the exact spherical volume nor the blurring due to the PSF can be considered with their approach when fluorescence intensities for different evanescent excitations are calculated.

Secretory granules have a dense internal protein matrix. Thus the evanescent wave may penetrate them in a way that is different from the way in which it penetrates the surrounding solution. This problem has been treated by a theoretical and a practical investigation, with the result that the internal fields inside the vesicles can be assumed to be equal to the outside evanescent field.

Determining distances and diameters of granules

Because of intrinsic measurement errors, significantly more than three measurements were necessary to determine the three unknown parameters encoding the measured fluorescence. Such errors in the measured intensity are due to 1) background fluorescence arising from vesicles located deeper in the cell, 2) photon noise, 3) a peak intensity of the spot instead of the whole spot intensity, 4) an error in the surface intensity due to finite accuracy of the setup, and 5) the mentioned lateral scattering of excitation light. Not all errors could be minimized, such as the recorded intensity of the spots, where the overlap of adjacent spots made a separation and assignment very difficult.

For the determination of vesicle distances, it was important to determine the dependency of the fluorescence on the distance a of extended spheres (100–500 nm in diameter) moving along the z direction. Using modeled data, we found after integration over the z extension (thus averaging in intensity) that larger objects showed an approximately exponential decrease in fluorescence intensity when their center distance to the interface was enlarged (Fig. 6). This is different for a point object that moves away from $z = 0$ nm (see also Fig. 3 *a*). To reduce the number of unknown parameters (a, R, c), we calculated the concentration-independent ratio of two intensities for granule spots at different penetration depths. Furthermore, a mean granule radius $R =$ 180 nm was assumed, which led, according to the mathematical model, to a maximum relative intensity error of 20%. In addition, a linear approximation of the exponential dependency between center distance a and intensity $I(a)$

was justified for granule distances $a < (d_{12} + R) \approx 400$ nm. Subtraction of background fluorescence led to further errors of the spot intensities, yielding a relative error in granule distances of up to 50%. This error might appear to be rather large, but it is at least "half the truth" in comparison to analyses where distances are determined with single-exponential decay. This is definitely not possible as long as the internal fluorophore concentration varies between granules. The present study investigated the possibility of determining distances of secretory granules with MAEW. The answer, however, should be that there are easier and more accurate methods (with, for example confocal microscopy) of determining positions of resting granules in living cells (provided the biological processes are slow). If, on the other hand, size and dye concentration are constant or a scattering of the evanescent wave can be avoided, conventional TIRFM and MAEWM still represent powerful microscopy techniques. Furthermore, the effects of photobleaching and photodamage are much smaller in MAEWM, because the fluorescence excitation volume (bleaching volume) is significantly smaller than the detection volume. In confocal microscopy, the excitation volume is about $(2^{1/2})^3 \approx 3$ times larger.

Beyond the limits of confocal microscopy, MAEW microscopy is able to resolve spheres 50–300 nm in diameter, by a stepwise recording of a Laplace transform. By calculating the inverse transform, a z resolution of $\sim$10 nm is possible (in a conventional microscope the inverse Fourier transform is performed by the tube lens). Because we took isolated granules adhering to the interface, the center distance a was equal to the granule radius R. We eliminated the concentration c by building the ratio of two spot intensities: the intensity $I(d)$ as a function of penetration depth d was normalized to the intensity $I(d = 100\ \text{nm})$. Furthermore, the whole spot intensity could be determined because no overlap of spots occurred. As shown in the Results, the diameters of three different granules were reconstructed after 19 measured and normalized fluorescence intensities $I_d/I_{d=100}$ were plotted as a function of penetration depth d. By χ^2 minimization, a theoretical curve was fitted to the noisy data, consisting of 19 values for each granule. The fit revealed diameters of 70 nm, 240 nm, and 300 nm. The χ^2 error was small; the data fitted well to the model. We establish that this method is complementary to determining diameters of granules with high-resolution confocal microscopes.

Is it possible to determine the radius R and the position a of a granule simultaneously? If a resolution better than 80 nm is required, the answer is no. In a plot of $I(d)$ the fluorescence intensity against the penetration depth, both the radius R and the center distance a are determined via the slope of the curve $I(d)$. According to our model small granules at a short distance and large granules at a longer distance have a very similar dependency $I(d)$.

SUMMARY

In this study a fluorescence excitation technique using variable penetration depths of evanescent waves was developed; this technique was then applied to investigate secretory granules in live chromaffin cells. The major boundary conditions for the optical and electronic setup were speed, on the one hand, and, on the other, a minimum number of optical elements to be aligned. We illustrated and explained the principal problems of excitation with evanescent waves; special demands on detection optics were pointed out. A comparison of theoretical models for fluorescence volumes of spherical granules with actual measurements of the spot intensities was carried out to determine the distances from granules in cells to the coverslip as well as the diameters of isolated granules.

APPENDIX: BACKGROUND SUBTRACTION

The background fluorescence $U(x, y)$ is subtracted from every picture $I(x, y)$ by high-pass Gauss filtering. Here the cutoff frequency is determined by the spot diameter of granules close to the interface. The superscripts in the relation $I^+(x, y) = I^-(x, y) + U(x, y)$ describe the intensity before (+) and after (−) background subtraction. We write for the quotient of two pictures I_1 and I_2

$$\frac{I_1^-(x,y)}{I_2^-(x,y)} = \frac{I_1^+(x,y) - U_1(x,y)}{I_2^+(x,y) - U_2(x,y)} \approx \exp\left(-a \Big/ \frac{d_1 \cdot d_2}{d_1 + d_2}\right) \quad \text{(A1)}$$

As the filtered distribution $I_2^-(x, y)$ has zeros, we expand the denominator to a series:

$$\frac{I_1^-}{I_2^-} = \frac{I_1^+ - U_1}{I_2^+} \cdot \frac{1}{1 - U_2/I_2^+} = \frac{I_1^-}{I_2^+} \cdot \left\{1 - \frac{U_2}{I_2^+} + \left(\frac{U_2}{I_2^+}\right)^2 - \cdots\right\} \quad \text{(A2)}$$

Higher orders of the series can be omitted.

This work was supported by the Max Planck Society. The author thanks J. Steyer and W. Almers for fruitful discussions and practical help, I. Wunderlich for cell culture, J. Tritthardt for support with electronic problems, J. Pauli for building special mechanical components, and B. Ölveczky for the calculation of $Q(z)$. Further thanks to E. H. K. Stelzer, J. White, J. Swoger, N. Salmon, and R. Hodge for carefully reviewing and discussing the manuscript.

REFERENCES

Albillos, A., G. Dernick, H. Horstmann, W. Almers, G. Alvarez de Toledo, and M. Lindau. 1997. The exocytotic event in chromaffin cells revealed by patch amperometry. *Nature.* 389:509–512.

Almers, W. 1990. Exocytosis. *Annu. Rev. Physiol.* 52:607–624.

Arfken, G. B., and H. J. Weber. 1995. Mathematical Methods for Physicists, 4th Ed. Academic Press, San Diego. 877.

Axelrod, D. 1981. Cell substrate contacts illuminated by TIRF. *J. Cell Biol.* 89:141–145.

Axelrod, D., E. H. Hellen, and R. M. Fulbright. 1992. Total internal reflection fluorescence. *In* Topics in Fluorescence Spectroscopy: Principles and Applications, Vol. 3. Biochemical Applications. J. Lakowicz, editor. Plenum Press, New York. 289–343.

Burghardt, T. P., and N. L. Thompson. 1984. Effects of planar dielectric interfaces on fluorescence emission and detection. *Biophys. J.* 46: 729–737.

Burmeister, J. S., G. A. Truskey, and W. M. Reichert 1994. Quantitative analysis of variable-angle total internal reflection fluorescence microscopy (VA-TIRFM) of cell/substrate contacts. *J. Microsc.* 173:39–51.

Carniglia, C. K., L. Mandel, and K. H. Drexhage. 1972. Absorption and emission of evanescent photons. *J. Opt. Soc. Am.* 62:479–486.

Chew, H., D.-S. Wang, and M. Kerker. 1979. Elastic scattering of evanescent electromagnetic waves. *Appl. Opt.* 18:2679–2687.

Denk, W., J. H. Strickler, and W. W. Webb. 1990. Two-photon laser scanning fluorescence microscopy. *Science.* 248:73–76.

Hecht, E. 1987. Optik, 2nd Ed. Addison-Wesley, New York. 104–108, 429.

Hellen, E. H., and D. Axelrod. 1986. Fluorescence emission at dielectric and metal-film interfaces. *J. Opt. Soc. Am. B.* 4:337–350.

Inoue, S. 1987. Video Microscopy. Plenum Press, New York.

Knight, J. C. 1995. Mapping whispering gallery modes in microspheres with a near-field probe. *Optics Lett.* 20:1515–1517.

Lukosz, W., and R. E. Kunz. 1977. Light emission by magnetic and electric dipoles close to a plane interface. I. Total radiated power. *J. Opt. Soc. Am.* 67:1607–1614.

Oheim, M., D. Loerke, B. Preitz, and W. Stuehmer. 1998a. A simple optical configuration for depth-resolved imaging using variable angle evanescent-wave microscopy. *SPIE.* 3568:131–140.

Oheim, M., D. Loerke, W. Stuehmer, and R. H. Chow. 1998b. The last few milliseconds in the life of a secretory granule. Docking, dynamics and fusion visualized by total internal reflection microscopy (TIRFM). *Eur. Biophys. J.* 27:83–98.

Ölveczky, B. P., N. Periasamy, and A. S. Verkman. 1997. Mapping fluorophore distributions in three dimensions by quantitative multiple angle-total internal reflection fluorescence microscopy. *Biophys. J.* 73: 2836–2847.

Parsons, T. D., J. R. Coorssen, H. Horstmann, and W. Almers. 1995. Docked granules, the exocytic burst, and the need for ATP hydrolysis in endocrine cells. *Neuron.* 15:1085–1096.

Pawley, J. B. 1995. Handbook of Biological Confocal Microscopy, 2nd Ed. Plenum Press, New York.

Prieve, D. C., and J. Y. Walz. 1993. Scattering of an evanescent surface wave by a microscopic dielectric sphere. *Appl. Optics.* 32:1629–1641.

Reichert, W. M., and G. A. Truskey. 1990. Total internal reflection fluorescence (TIRF) microscopy. I. Modelling cell contact region fluorescence. *J. Cell Sci.* 219–230.

Rohrbach, A. 1998. Optische Anregung und Detektion biologischer Fluoreszenzobjekte hinter dielektrischen Grenzflächen. Dissertation, Heidelberg.

Rohrbach, A., and W. Singer. 1998. Scattering of a scalar field at dielectric surfaces by Born series expansion. *J. Opt. Soc. Am. A.* 15:2651–2659.

Stelzer, E. H. K., and S. Lindek. 1994. Fundamental reduction of the observation volume in far-field light microscopy by detection orthogonal to the illumination axis: confocal theta microscopy. *Opt. Commun.* 111:536–547.

Steyer, J. A., H. Horstmann, and W. Almers. 1997. Transport, docking and exocytosis of single secretory granules in chromaffin cells. *Nature.* 388:474–478.

Stout, A. L., and D. Axelrod. 1989. Evanescent field excitation of fluorescence by epi-illumination microscopy. *Appl. Optics.* 28:5237–5242.

Vitale, M. L., E. P. Seward, and J.-M. Trifaro. 1995. Chromaffin cell cortical actin network dynamics control the size of the release-ready vesicle pool and the initial rate of exocytosis. *Neuron.* 14:353–363.